Competing soft dielectric phases and detailed balance in thin film manganites

Patrick R. Mickel, Amlan Biswas, and Arthur F. Hebard
Department of Physics, University of Florida, Gainesville, Florida 32611, USA
(Received 16 March 2011; revised manuscript received 17 August 2012; published 7 September 2012)

Using frequency dependent complex capacitance measurements on thin films of the mixed-valence manganite $(La_{1-y}Pr_y)_{1-x}Ca_xMnO_3$, we identify and resolve the individual dielectric responses of two competing dielectric phases. We characterize their competition over a large temperature range, revealing they are in dynamic competition both spatially and temporally. The phase competition is shown to be governed by the thermodynamic constraints imposed by detailed balance. The consequences of the detailed balance model strongly support the notion of an "electronically soft" material in which continuous conversions between dielectric phases with comparable free energies occur on time scales that are long compared with electron-phonon scattering times.

DOI: 10.1103/PhysRevB.86.094410 PACS number(s): 75.47.Lx, 73.20.Mf, 73.50.Gr, 77.22.Gm

I. INTRODUCTION

Phase separation and phase competition are associated with many of the most exotic material properties that complex oxides have to offer and are found ubiquitously in high-temperature superconductors,[1,2] spinels,[3] multiferroics,[4,5] and mixed-valence manganites.[6,7] Accordingly, understanding the fundamental mechanisms of phase separation/competition is necessary for the technological implementation of these next generation materials. In mixed-valence manganites, the disorder[8] and strain[9] based explanations have recently been augmented by a model describing an "electronically soft" coexistence, where the phase separation is driven by delocalized thermodynamic physics.[10] This theory has broad implications for complex oxides with coexisting and competing phases,[11–13] however, evidence for "electronically soft" phases has yet to be provided.

In this report we utilize frequency-dependent dielectric measurements of thin films of the mixed phase manganite $(La_{1-y}Pr_y)_{0.67}Ca_{0.33}MnO_3$ (LPCMO) to separately identify charge ordered insulating (COI) and paramagnetic insulating (PMI) phases and then to provide a spatial and temporal description of the dynamic competition between these phases over a broad temperature range. We find that the constraints imposed by detailed balance strongly support the notion of an "electronically soft" material, as we observe continuous conversions of dielectric phases with comparable free energies competing on time scales that are long compared with electron-phonon scattering times.

II. EXPERIMENTAL

A. Sample fabrication

Our sample geometry comprises a (110) oriented $NdGaO_3$ substrate, a 30-nm-thick epitaxial thin film $(La_{1-y}Pr_y)_{0.67}Ca_{0.33}MnO_3$ (with $y \approx 0.5$) bottom electrode grown by pulsed laser deposition, a 10-nm-thick AlO_x dielectric grown by RF-sputtering, and a 50-nm-thick Al top electrode grown by thermal deposition [see the inset of Fig. 1(a)]. The (110) oriented substrate was chosen since it is well lattice matched to LPCMO. Four additional samples with thicknesses in the range 30 nm to 150 nm have shown similar results to those reported here. For further details on fabrication of the $(La_{1-y}Pr_y)_{0.67}Ca_{0.33}MnO_3$ films, see Ref. 14.

B. Impedance measurements

The *ab* plane resistance of the LPCMO film was measured using a four probe geometry, sourcing current, and measuring voltage. The temperature dependence of the resistance is shown in Fig. 1, demonstrating that with decreasing temperature T the resistance increases smoothly until $T = 115$ K, and then decreases as an expanding ferromagnetic metallic (FMM) phase forms a percolating conducting network[6,7] at the expense of the insulating dielectric phases. In bulk LPCMO samples there is also a signature kink in $R(T)$ in the range 200–220 K (interpreted as the temperature where the COI phase becomes well established[15–17]) which is absent here, suggesting the COI phase is not present. However, as described below, our complex capacitance measurements demonstrate an increased sensitivity to dielectric phases compared to the dc resistance, and convincingly confirm the presence of the COI phase.

Dielectric measurements are made on the LPCMO film using the trilayer configuration discussed above in which the manganite serves as the base electrode. Using this technique, which enables the study of leaky dielectrics by blocking shorting paths (see Ref. 18, Sec. III A and Appendix for a detailed discussion), we measure the complex capacitance over the bandwidth 20 Hz to 200 kHz and the temperature range $100\ \text{K} < T < 300\ \text{K}$ using an HP4284 capacitance bridge. The capacitance was sequentially sampled at 185 frequencies spaced evenly on a logarithmic scale across our bandwidth as the temperature was lowered at a rate of 0.1 K/min, thus guaranteeing a complete frequency sweep over every 0.25 K temperature interval. The capacitances of individual frequencies were then interpolated onto a standard temperature grid with steps of 1 K for each frequency, allowing each dielectric spectrum to be analyzed at constant temperature. As a check, the interpolated capacitance values from the multiple-frequency temperature sweep were compared to single-frequency temperature sweeps at several representative frequencies across the bandwidth, and were found to be identical. Warming runs were also performed with no qualitative change in model parameters other than a hysteretic shift in temperature.

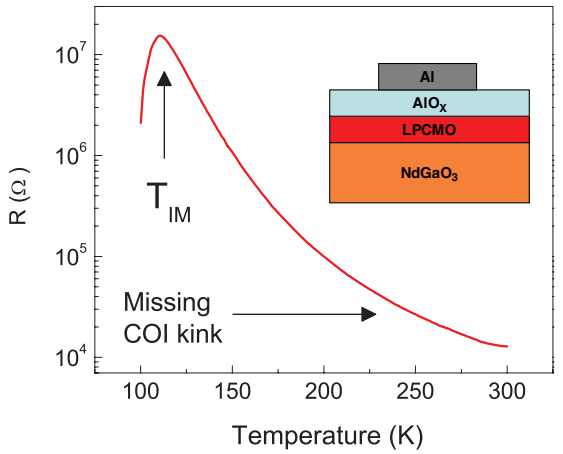

FIG. 1. (Color online) Resistance and sample geometry. The *ab* in-plane resistance (measured upon cooling) shows a pronounced peak at the insulator-to-metal transition $T_{IM} \approx 115$ K, but lacks a COI associated anomaly seen in bulk manganites in the temperature range 200–250 K (Refs. 15–17). Inset: Sample geometry, where the LPCMO film is the bottom electrode of a trilayer capacitor structure.

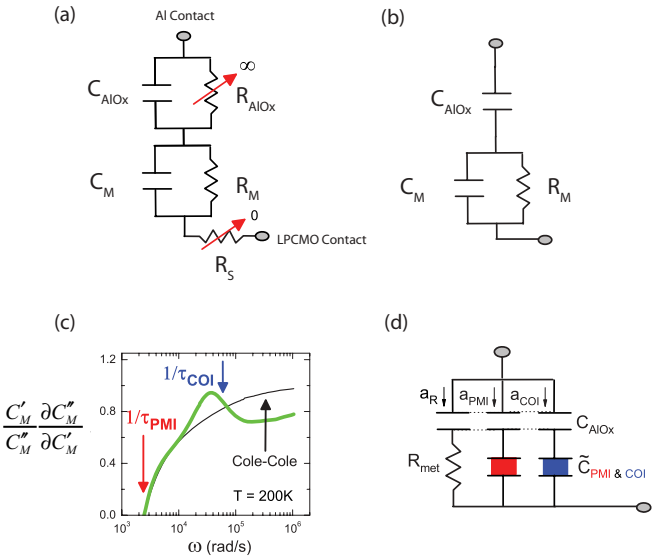

FIG. 2. (Color online) Circuit models. (a) Circuit model composed of a Maxwell-Wagner circuit with a series resistance (R_s) component that accounts for the in-plane voltage drop along the film. In select frequency ranges, this in-plane voltage drop can be shown to be negligible compared to the *c*-axis voltage drops across the capacitors, effectively removing R_s from the circuit (Ref. 18). Additionally, the AlO_x dc resistance is exceptionally large and can be approximated as infinite. (b) The resulting circuit model for our measurement bandwidth after approximations and limits are applied. See the Appendix for a complete discussion of the relevant time scales. (c) The logarithmic parametric slope, $(C'_M/C''_M)(\partial C''_M/\partial C'_M)$ (green), is shown to differ from the Cole-Cole (Ref. 20) dielectric response, providing a signature of multiple phases. (d) Circuit model incorporating the complex dielectric function of C_M, which has multiple components. Three parallel components, C_{PMI}, C_{COI}, and R_{met}, are in series to fractional areas of the AlO_x layer.

III. ANALYSIS

A. Circuit model

Figure 2 shows the circuit model used to interpret the dielectric data. The basic treatment of the circuit model was introduced in Ref. 18, however we review and expand upon its application here. In contrast to the resistance measurements of Fig. 1 where four contacts are made directly to the LPCMO, the dielectric measurements are two terminal, with one contact to the Al electrode and the other to the edge of the LPCMO film. In this configuration the sample geometry can be represented by a series resistance R_S, through which in-plane currents flow from the LPCMO contact to the capacitor structure which comprises a Maxwell-Wagner circuit combination of two series-connected parallel combinations of resistors and capacitors. The voltage drops across the respective capacitances of the LPCMO and AlO_x films are in the *c*-axis direction, perpendicular to the plane of the substrate. Reference 18 introduced a set of frequency-dependent impedance constraints which guarantee that in our measurement bandwidth the in-plane voltage drop across R_S is negligible compared to the *c*-axis voltage drops, thus effectively removing R_S from the circuit. The net result is that the equipotential planes corresponding to the measured voltages are parallel to the film-substrate interface and thus sensitive to the *c*-axis capacitance. This is important because it places the AlO_x layer (with approximately infinite resistance) directly in series with the *c*-axis capacitance of the manganite film.

The resulting circuit is shown in Fig. 2(b), a parallel capacitor and resistor (associated with the manganite capacitance and dc resistance) in series with a capacitor (associated with the AlO_x layer). The complex capacitance of this total circuit can then be written as

$$C^* = \frac{C_{\mathrm{AlO}_x}}{1 + \left(i\omega R_M C_{\mathrm{AlO}_x}\right)/(1 + i\omega R_M C_M)}, \qquad (1)$$

where C_{AlO_x} is the capacitance of the AlO_x layer, C_M is the capacitance of the manganite film, R_M is the shorting dc resistance of the manganite film, and $\omega = 2\pi f$ where f is the measurement frequency. At sufficiently high frequency (i.e., when $\omega R_M C_M \gg 1$), the capacitance of the circuit may be written as

$$C^* = \frac{C_{\mathrm{AlO}_x} C_M}{C_{\mathrm{AlO}_x} + C_M}, \qquad (2)$$

and if $C_M \ll C_{\mathrm{AlO}_x}$, as it is in our system, then $C^* \approx C_M$. We note that C_M is a complex capacitance which may display dispersion, but its frequency dependence is independent of R_M.

The circuit in Fig. 2(b) has three dominant time scales (or frequency ranges). At the longest time scales, the circuit is dominated by the AlO_x layer and $C^* \approx C_{\mathrm{AlO}_x}$ [this can be seen by setting $\omega = 0$ in Eq. (1) above]. At intermediate time scales, where $1/\omega \approx R_M C_{\mathrm{AlO}_x}$, the circuit is sensitive only to C_{AlO_x} and R_M. At time scales shorter than $R_M C_M$, the capacitance is sensitive only to C_M, and is independent of the parallel shorting resistor R_M and the AlO_x capacitance C_{AlO_x}. Finally, at high frequency the in-plane voltage drop across the series resistance dominates. For an in-depth discussion of the relevant time scales for the circuit in Fig. 2(b) and the role of the series resistance R_S, see the Appendix.

Reference 18 shows a clear crossover between these three time scales/frequency ranges, and demonstrates that our measurements are made in the high frequency range, where the capacitance is sensitive only to the inherent dielectric properties of the manganite film C_M and not its dc resistance R_M. Therefore, the time dependence reported is not the result of RC time constants (these occur at lower frequencies), but rather intrinsic relaxation time scales. Said in another way, there is an essential difference between a "lossy" capacitor (C_M), which is complex and includes the real and imaginary parts of polarization response, and a "leaky" capacitance (C_M in parallel with R_M), which provides a shunting path for dc currents. As explained above, the choice of frequency range in our experimental configuration allows us to ignore the contributions of currents flowing through both R_S and R_M and thus measure the inherent dielectric relaxation of the LPCMO film.

Analyzing the frequency response of the manganite capacitance (C_M) reveals a high-frequency anomaly as shown in Fig. 2(c), which compares our capacitance data to the ubiquitous[19] Cole-Cole dielectric response[20] of standard dielectric theory. Plotting the logarithmic parametric slope versus frequency, $[\partial(\ln C''_M)/\partial\omega]/[\partial(\ln C'_M)/\partial\omega]$ (where C'_M and C''_M are the real and imaginary capacitances with $C'' = 1/\omega R_P$ directly related to the parallel resistance R_P reported by the capacitance bridge), the Cole-Cole response increases monotonically while our data display a high-frequency non-monotonic anomaly. The zero crossing in Fig. 2(c) represents the loss peak (see also Fig. 3) of the PMI phase, and considering the phase coexistence found in bulk, we postulate that the high frequency anomaly in C_M is due to a higher frequency dielectric relaxation of the COI phase.

To test our hypothesis that the COI phase is responsible for the high frequency anomaly, we modify the circuit model of Ref. 18 to account for multiple phases. Figure 2(d) shows the modified circuit in which C_M encompasses phase coexistence. It is composed of three parallel components all in series to fractional areas of the AlO_x dielectric layer: $a_{\rm COI}$, $a_{\rm PMI}$, and a_R (the fractional area of the FMM phase, which acts as a resistive short at low temperatures), with the constraint $\sum a_i = 1$. Placing the capacitances of each phase in parallel requires that the domains of each phase span the film thickness, thus obviating a series configuration. Our film thickness of 30 nm, however, likely satisfies this requirement, as the phase domains of manganites in multiple phase separation states have been shown to be on the order of microns.[6,7] Above T_{IM}, $a_R \approx 0$, and the circuit is dominated by $C_{\rm PMI}$ and $C_{\rm COI}$ in our frequency range, so that the total dielectric response may be approximated by the superimposition of two Cole-Cole dielectric functions,

$$\tilde{\epsilon}(\omega) = \epsilon_\infty + \frac{A_{\rm PMI}}{1+(i\omega\tau_{\rm PMI})^{1-\alpha}} + \frac{A_{\rm COI}}{1+(i\omega\tau_{\rm COI})^{1-\beta}}, \tag{3}$$

where the amplitudes A_i are the product of the fractional area a_i and dielectric constant ϵ_i of each phase [$A_i = a_i(\epsilon_i - \epsilon_{\infty,i})$], ϵ_∞ includes the infinite frequency response of both dielectric phases, $\tau_{\rm COI}$ and $\tau_{\rm PMI}$ are the respective relaxation time scales, and α and β are the respective dielectric broadenings.

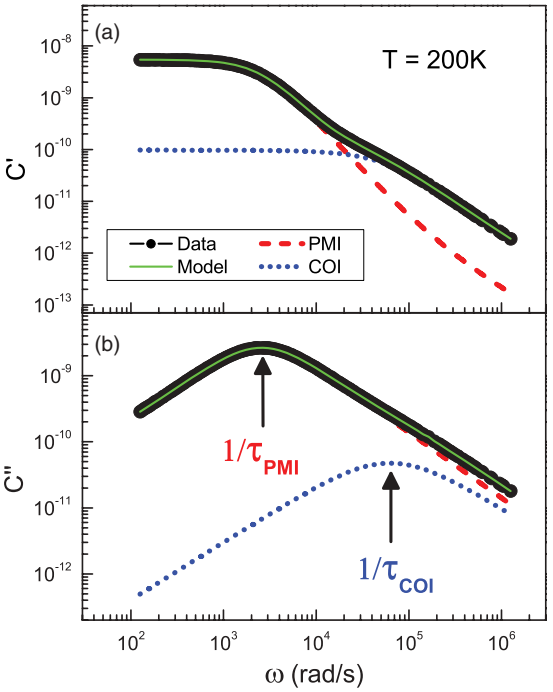

FIG. 3. (Color online) Parallel circuit model describes complex capacitance data. (a) The measured real capacitance (black) is compared with fits to Eq. (3) (green) at $T = 200$ K. (b) Measured imaginary capacitance. The individual capacitances of the PMI (red dash) and COI (blue dot) phases are also shown. At low frequencies, the PMI phase dominates both channels, and at high frequencies the COI dominates in the real channel, but not the imaginary channel. This mixing of relaxation components at high frequencies results in the logarithmic parametric-slope behavior seen in Fig. 2(c).

We quantitatively model C_M with Eq. (3) using the fixed temperature dielectric spectrums, varying $\omega = 2\pi f$ over 185 frequencies over the bandwidth 20 Hz to 200 kHz (see Sec. II B). The bandwidth was chosen such that at the lowest frequencies Eq. (2) is still valid, and that at the highest frequencies the in-plane ab plane series resistance R_S can still be ignored. The fits are produced by simultaneously minimizing the difference between the measured complex capacitance and both the real and imaginary parts of Eq. (2). Figure 3 shows a typical fit, where the average relative error is less than 10^{-3}. In the low-frequency limit, $\epsilon(0) \approx A_{\rm PMI} + A_{\rm COI}$, allowing a fitting variable to be eliminated by reparameterizing the dielectric amplitudes in terms of their ratio, $r_{\rm amp} = A_{\rm COI}/A_{\rm PMI}$, and the measured $\epsilon(0)$, i.e., $A_{\rm PMI} = \epsilon(0)/(1+r_{\rm amp})$ and $A_{\rm COI} = r_{\rm amp}\epsilon(0)/(1+r_{\rm amp})$. As $\tau_{\rm PMI}$ is determined from the low-frequency loss peak and ϵ_∞ is vanishingly small [see Figs. 2(c) and 3(b)], four free variables are determined by the fits: $r_{\rm amp}$, α, β, and $\tau_{\rm COI}$. We fit our complex capacitance data to this five-parameter model [Eq. (3)] at fixed temperatures in 1 K steps between 100 K and 300 K. Analyzing the temperature dependence of the model parameters permits the identification of the phases, and provides a detailed spatial and temporal characterization of their coexistence/competition.

B. Temperature dependence of model parameters

Dielectric broadening provides a measure of the correlations among relaxors, and it is known that the COI phase is a highly correlated and ordered phase. Thus, it is expected that the broadening of the COI phase should increase as the phase forms. The temperature dependence of β displays these charge-ordering features [see Fig. 4(a)], while α is featureless, thereby identifying the high-frequency response as the COI dielectric phase. As seen in Fig. 3, the COI phase dominates the high-frequency response of the real capacitance, but only contributes slightly to the imaginary capacitance. Thus, the high frequency features of the logarithmic parametric slope [seen in Fig. 2(c)] are the result of a mixture of the real component of the COI phase and the imaginary component of the PMI phase, and are a signature of phase separation. Figure 4 also shows the temperature dependence of the ratio of dielectric amplitudes (discussed in detail below).

Figure 5 shows Arrhenius plots of τ_{PMI} and τ_{COI} over the temperature range 100 K $< T <$ 350 K. Surprisingly, over the linear regions, the activation energies of each phase are nearly equal, with $E_A(\mathrm{PMI}) = 117.9 \pm 0.2$ meV and $E_A(\mathrm{COI}) = 118.6 \pm 0.3$ meV. These values are consistent with small polarons, the known conduction and polarization mechanism in manganites.[21,22]

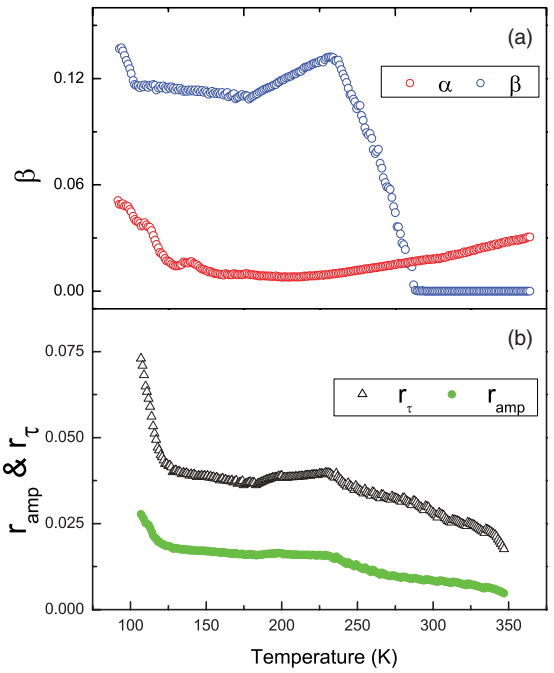

FIG. 4. (Color online) Temperature dependence of selected model parameters identifies phases and verifies detailed balance. (a) The temperature dependence of β is shown to match the temperature dependence of the correlations of COI phase, where COI nanoclusters are reported in a related material to appear near 280 K with the phase fully developed below 240 K (Ref. 17), identifying the high-frequency relaxation as the COI phase. The broadening of the PMI phase α is shown to be featureless in this temperature range. (b) The temperature dependence of the ratios of the dielectric amplitudes, $r_{\mathrm{amp}} = a_{\mathrm{COI}}/a_{\mathrm{PMI}}(\epsilon_{\mathrm{COI}}/\epsilon_{\mathrm{PMI}})$, and time scales, $r_\tau = \tau_{\mathrm{COI}}/\tau_{\mathrm{PMI}} = a_{\mathrm{COI}}/a_{\mathrm{PMI}}$, are compared. As discussed in the text, the strong correlation between the ratios confirms that the phase competition is governed by detailed balance.

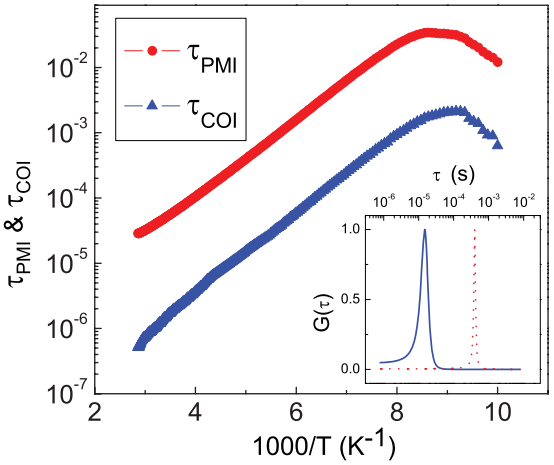

FIG. 5. (Color online) Region of identical activation energies provides clue for detailed balance. Arrhenius plots are shown for τ_{COI} and τ_{PMI}, with $E_A \approx 118$ meV in the linear region for both dielectric phases. The nearly identical E_A's suggest the phases share a single energy barrier [depicted in the middle panel of Fig. 6(b)]. Inset: The distributions of hopping-rate time scales are shown to be narrow for both phases, suggesting temporally coherent hopping (PMI dotted red, and COI solid blue).

C. Detailed balance

The strikingly similar activation energies of the two phases suggests the relaxations are coupled, possibly sharing a common energy barrier. Crossing this energy barrier would result in the two phases converting into each other. In our system, however, each dielectric also polarizes independently without converting into the other phase. Therefore, the phases must be connected through a common excited state from which relaxations can occur to either phase. This common state is consistent with adiabatic polaron hopping in manganites,[21] where the lattice relaxes slowly in response to fast electronic hopping (a polaron is a quasiparticle that includes an electron and the lattice distortion caused by its presence).

We model this process in our samples by the three state system shown in Fig. 6. The electrons of the polarons of both dielectric phases absorb thermal fluctuations that activate them over their hopping barriers to an equivalent "excited" state: a relocated electron surrounded by a lattice site that has yet to relax. The new lattice site has some initial distortion (either PMI or COI), but as it accommodates the new electron it can transform/relax into distortions that correspond to either dielectric phase. The electronic hopping happens at characteristic rates which we measure directly from loss peak positions in the complex capacitance ($\gamma_P = 1/\tau_{\mathrm{PMI}}$ and $\gamma_C = 1/\tau_{\mathrm{COI}}$). The lattice site relaxation, however, occurs at unknown rates γ_E and γ'_E for the PMI and COI phases, respectively. This process effectively results in two channels, one in which polarization is manifested independently in each phase by polarons relocating without altering their distortions, and one in which polarons relocate as well as transforming their distortion state.

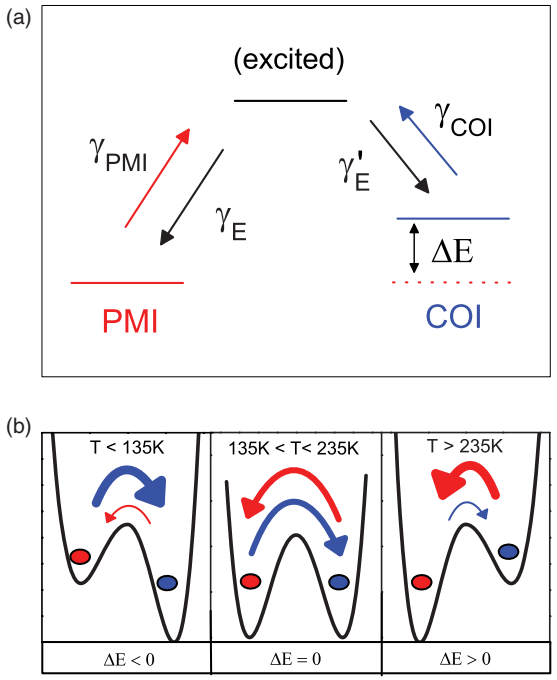

FIG. 6. (Color online) Detailed balance model. (a) An energy level schematic of a three state system describing the polaron hopping process is presented. Polarons of both dielectric phases absorb thermal fluctuations and hop to an excited state at their characteristic rates, $\gamma_{\rm PMI}$ and $\gamma_{\rm COI}$. The excited state is equivalent for both phases, corresponding to an electron surrounded by an undistorted lattice. The lattice can then relax into distortion states that correspond to polarons of either dielectric phase. (b) Schematic depiction of the temperature evolution of detailed balance and the energy barriers separating the PMI and COI dielectric phases.

Since the equilibrium populations of each phase are constant in time, the rate equations for the three state model in Fig. 6 are given by

$$\frac{\partial}{\partial t}\begin{pmatrix} n_P \\ n_E \\ n_C \end{pmatrix} = \begin{pmatrix} -\gamma_P & \gamma_E & 0 \\ \gamma_P & -(\gamma_E+\gamma'_E) & \gamma_C \\ 0 & \gamma'_E & -\gamma_C \end{pmatrix}\begin{pmatrix} n_P \\ n_E \\ n_C \end{pmatrix}, \quad (4)$$

where n_P, n_C, and n_E are the populations of the PMI, COI, and excited state, respectively. Solving this system of equations at equilibrium results in a detailed balance equation of the form

$$n_C(\gamma_C\gamma_E) = n_P(\gamma_P\gamma'_E), \quad (5)$$

where $(\gamma_C\gamma_E)$ and $(\gamma_P\gamma'_E)$ are the effective transition probabilities of each phase. Although the populations of each phase are time independent at equilibrium, they still have inherent temperature and energy dependences governed by Boltzmann statistics. The populations of each phase may be written in terms of their ground-state population and an exponential factor,

$$\begin{aligned} n_P &= n_P^0 e^{-E_{\rm PMI}/kT} \\ n_C &= n_C^0 e^{-E_{\rm COI}/kT}, \end{aligned} \quad (6)$$

where $E_{\rm PMI}$ and $E_{\rm COI}$ are the configuration energies of each phase. We stress here the distinction of $E_A(i)$ and E_i with $i = $ PMI,COI. $E_A(i)$ is the energy barrier to hopping, and is thus the energy difference between the current polaron state and the excited energy state: $E_A(i) = E_{\rm excited} - E_i$ with $i =$ PMI,COI. The detailed balance equation may then be rewritten as

$$\left(n_C^0/n_P^0\right)e^{-\Delta E/kT} = (\tau_{\rm COI}/\tau_{\rm PMI})(\gamma'_E/\gamma_E), \quad (7)$$

where $\Delta E = E_{\rm COI} - E_{\rm PMI}$ is the difference in configuration energy between phases.

By making the physically reasonable ansatz that the ratio of populations is equal to the ratio of fractional areas (i.e., volumes for constant thickness),

$$\left(n_C^0/n_P^0\right)e^{-\Delta E/k_BT} = a_{\rm COI}/a_{\rm PMI}, \quad (8)$$

our circuit model provides a direct test of the detailed balance constraint of Eq. (7). Figure 4(b) shows the temperature dependence of the *independently determined* ratios, $r_\tau = \tau_{\rm COI}/\tau_{\rm PMI}$ and $r_{\rm amp} = (a_{\rm COI}/a_{\rm PMI})(\epsilon_{\rm COI}/\epsilon_{\rm PMI})$. The two ratios follow a similar trend with a ratio of ratios, $r_\tau/r_{\rm amp} = (\tau_{\rm COI}/\tau_{\rm PMI})(a_{\rm PMI}/a_{\rm COI})(\epsilon_{\rm PMI}/\epsilon_{\rm COI}) \approx 2.4$ over the displayed temperature range.

Combining Eqs. (7) and (8) leads to the simplified expression $r_\tau/r_{\rm amp} = (\epsilon_{\rm PMI}/\epsilon_{\rm COI})(\gamma_E/\gamma'_E)$, which is confirmed to be a constant with additional measurements for different thickness films of $\epsilon_{\rm COI}$ and $\epsilon_{\rm PMI}$ that are found to be in agreement with bulk values, providing the result $\gamma'_E/\gamma_E \approx 1$ (see below). The similarities in the temperature dependence of r_τ and $r_{\rm amp}$ in Fig. 3(b) thus confirm the constraints imposed by detailed balance.

Assuming the lattice relaxation rates are equal ($\gamma'_E/\gamma_E \approx 1$, this assumption is validated below), then according to Eqs. (7) and (8) the ratio of fractional areas is known. Knowledge of the ratio of fractional areas $a_{\rm COI}/a_{\rm PMI}$ and the ratio of dielectric amplitudes $A_{\rm COI}/A_{\rm PMI}$ together with the respective constraining normalizations, $a_{\rm COI} + a_{\rm PMI} = 1$ and $A_{\rm COI} + A_{\rm PMI} = \epsilon(0)$, allow an experimental determination of the respective dielectric constants $\epsilon_{\rm COI} = A_{\rm COI}/a_{\rm COI}$ and $\epsilon_{\rm PMI} = A_{\rm PMI}/a_{\rm PMI}$. Figure 7 shows the dielectric constants determined in this manner for four films with thickness ranging from 30 nm to 150 nm. The dielectric constants of each phase increase and saturate near their known bulk values[22–24] as the substrate strain relaxes. In manganites grown on NGO, the film is relaxed at a thickness of $d \approx 100$ nm[18,25] in agreement with the saturation of the data in the figure. The agreement of the data with these expectations tends to validate our assumption that $\gamma'_E/\gamma_E \approx 1$. In Ref. 18, these vertical strain gradients were shown to cause a shift in transition temperatures, however they were not found to effect the distribution of equipotentials within each sample.

The combination of Eq. (7) and Eq. (8) together with the result that $\gamma'_E/\gamma_E \approx 1$ leads to the relation $a_{\rm COI}\gamma_{\rm COI} \approx a_{\rm PMI}\gamma_{\rm PMI}$, which with the normalization $a_{\rm COI} + a_{\rm PMI} = 1$ gives the particularly simple relations,

$$a_{\rm COI} \approx \gamma_P/(\gamma_C+\gamma_P), \quad a_{\rm PMI} \approx \gamma_C/(\gamma_C+\gamma_P), \quad (9)$$

for the fractional areas occupied by each phase.

The consequences of our three state model as expressed in the above equations and illustrated in the schematic panels of Fig. 6(b) give a good description of the temperature evolution of the cooling data shown in Fig. 4(b). As the COI phase stabilizes with decreasing temperature ($T > 235$ K), its hopping

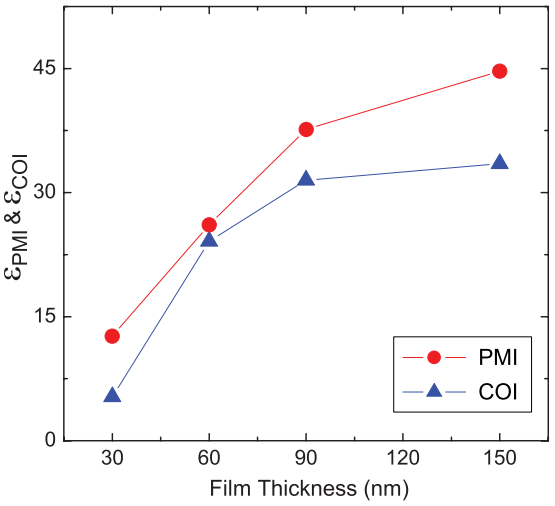

FIG. 7. (Color online) Thickness dependence of dielectric constants. The dielectric constants, calculated from the dielectric amplitudes and areas of each phase, $\epsilon_i = A_i/a_i$ (ignoring the vanishingly small $\epsilon_{\infty,i}$ of each phase), are shown to saturate near their bulk values once substrate strain is relaxed. The agreement with bulk data validates the areas calculated assuming equal lattice relaxation rates, $\gamma_E \approx \gamma'_E$.

rate decreases (polarons remain in the state longer because of a deeper potential well), increasing its population proportional to $e^{-\Delta E/kT}$, since $\Delta E \to 0$ as E_{COI} decreases. These population changes are depicted by the colored arrows, the size of which represent the magnitude of the respective transition rates. Then at intermediate temperatures ($135\ \mathrm{K} < T < 235\ \mathrm{K}$) the two phases are at equal energies ($\Delta E = 0$), making their relative populations temperature independent (equal size arrows and transition rates). Finally, at low temperatures the PMI phase destabilizes and ΔE decreases further and becomes negative as E_{PMI} increases [as shown in Fig. 6(b)], resulting in an increase of the COI population proportional to $e^{-\Delta E/kT}$.

D. Charge density waves

The original prediction of "electronically soft matter" describes the COI phase in terms of charge-density waves (CDW), and evidence for delocalized CDWs has been verified by multiple experimental techniques in manganites,[26–28] therefore, it is appropriate to discuss our data in this context. We first note that the absence of the COI transition in the resistance versus temperature curve (despite the observed phase competition) is analogous to similar behavior in CDW systems doped with large impurity densities.[29,30] The lack of a feature does not indicate the phases absence, rather it is the smearing of the COI transition by the inherent disorder and strain of thin films.[26] Furthermore, characterizing the temperature dependence of the PMI/COI competition reveals a highly correlated collective transport mode of the COI phase domains, similar to the "coherent creep" preceding "sliding" in CDW systems.[31]

The constraints of the parallel model [Fig. 2(d) and Eq. (3)] require that the hopping mechanism is correlated over sufficiently long length scales that regions equal to at least the film thickness hop together collectively, so that as the phases convert each phase boundary progresses simultaneously in a "creep" like manner. "Creep" is typically a random phenomenon, however, transforming our dielectric broadening to a distribution of time scales[32] (shown in the inset of Fig. 5), we find a narrow distribution of hopping rates suggesting an ordered process similar to the "temporally coherent creep" found in the CDW system $NbSe_3$.[31] The exact nature of the order is ambiguous, with two likely scenarios. The first possibility is the coherent propagation of phase domains, whereas the phase boundary "creeps" forward the regions behind synchronously hop, guaranteeing the continuity of the phase. The second scenario is a "breathing" mode in which the area of different phase domains cooperatively increase and decrease at a characteristic frequency (with total area conserved). Both scenarios demonstrate the collective and delocalized nature of the COI phase in which its entire charge distribution moves collectively and coherently in dynamic competition with the PMI dielectric phase.

IV. CONCLUSIONS

In summary, we have presented a dielectric characterization of the competition between the COI and PMI dielectric phases of $(La_{1-y}Pr_y)_{0.67}Ca_{0.33}MnO_3$, identifying signatures of phase separation and providing temperature dependent time scales, dielectric broadenings, and population fractions of each phase. More importantly, we demonstrate that the constraints imposed by detailed balance describe an "electronically soft" coexistence and competition between dielectric phases, highlighted by continuous conversions between phases on large length and time scales as well as a collective and delocalized nature of the charge-density distribution of the COI phase. Our findings provide important context concerning the fundamental mechanisms driving phase separation, and strongly support the concept of an "electronically soft" separation of delocalized competing thermodynamic phases.[10] Furthermore, we extend this concept to high temperature fluctuating phases which need not be ordered.

ACKNOWLEDGMENTS

The authors thank Tara Dhakal, Guneeta Singh-Bhalla, Chris Stanton, and Sefaatin Tongay for assistance with sample preparation as well as fruitful discussions. This research was supported by the US National Science Foundation under Grants No. DMR-1005301 (A.F.H.) and No. DMR 0804452 (A.B.).

APPENDIX

1. Sample geometry

Figure 8 shows the details of our thin film sample geometry and dimensions. Two separate electrode connections are shown: a four point Van der Pauw resistance configuration, and a two probe capacitance configuration. The four point Van der Pauw configuration, with two voltage and two current leads connected at the four sample corners, was used to measure the *ab* plane resistance shown in Fig. 1. The two point capacitance configuration is with the first electrode connected to the side

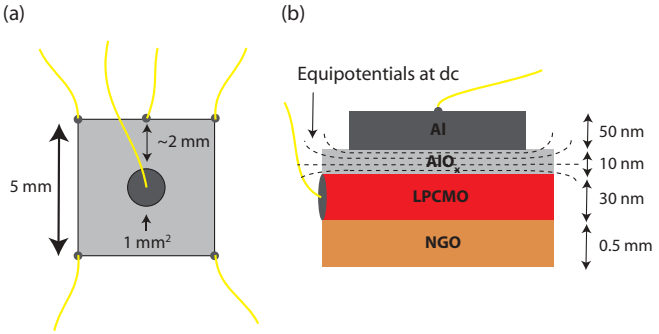

FIG. 8. (Color online) Sample geometry. (a) The dimensions and wire connections to our thin film sample are shown. The *ab* plane resistance measurements (see Fig. 1) are made using a four point Van der Pauw geometry with the voltage and current leads connected at the corners of the film. Capacitance measurements are made between the central circular electrode and the sample edge with average separation of ≈2 mm. (b) A cross section shows the thickness of each layer, with the LPCMO contact spanning the width of the LPCMO film. Equipotentials at dc are shown to be concentrated in the plane of the AlO_x layer.

of the manganite film and the second electrode connected to a circular top aluminum contact with ≈1 mm area. Figure 8(b) shows the composition and thickness of each layer of our sample, and illustrates that at dc the equipotentials are spaced vertically throughout the AlO_x film. Because of the large aspect ratio (electrode area of 1 mm^2 and dielectric thickness of 10 nm), edge effects can be ignored.

2. Series resistance analysis

Because our films are grown on an insulating substrate ($NdGaO_3$), electrical contact must be made to the side of the film, and the two-terminal capacitance measurement unavoidably represents a combination of both in-plane and perpendicular voltage drops. Depending on the size of the series resistance and the choice of measurement frequency, the in-plane voltage drop may dominate the measurement, leading to artifacts in the capacitance values. However, by comparing the components of the measurement circuit assumed by the capacitance bridge to be a simple parallel RC circuit model, constraints which guarantee that the perpendicular voltage drop dominates over the in-plane voltage drop can be derived.

The measurement circuit assumed by the capacitance bridge is shown in Fig. 9(a), and as mentioned above comprises a parallel configuration of a capacitor $C_B(\omega)$ and resistor $R_B(\omega)$. Figure 9(b) shows a simplified circuit model representative of our sample geometry: a resistance R_S, which determines the in-plane voltage drop, in series with the parallel combination of a complex (lossy) capacitor, $C^*(\omega) = C_1(\omega) - iC_2(\omega)$ with $R_2 = 1/[\omega C_2(\omega)]$, which together with the dc leakage resistor R_0 determines the perpendicular voltage drop. From our measurements of the two-terminal dc resistance we find that $R_0 + R_S > 10^{10}\ \Omega$. For values of R_S in the range 10^5–$10^7\ \Omega$ (see Fig. 1) this determines that negligible current flows through R_0, effectively removing it from the circuit. After this simplification, comparing the real and imaginary components

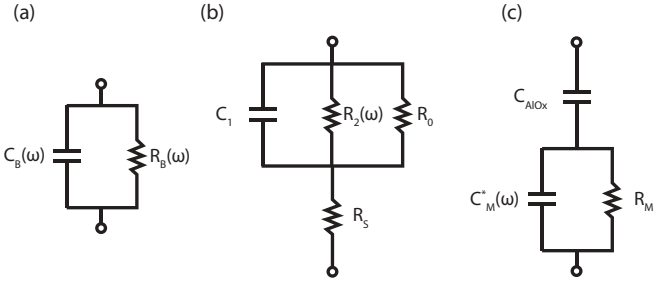

FIG. 9. Measurement circuit and circuit models. (a) The equivalent circuit, comprising the parallel combination of the measured capacitance C_B and resistance R_B, as reported by the capacitance bridge in "parallel" mode. (b) Circuit equivalent including the resistance R_S in series with the parallel combination of R_0, C_1, and R_2. The in-plane voltage drop is proportional to R_S whereas the perpendicular voltage drop is proportional to the complex impedance of the parallel combination of R_0, C_1, and R_2. (c) With the series resistance R_s ruled negligible, the complex capacitance is decomposed into a modified Maxwell-Wagner circuit of the manganite impedance and AlO_x capacitance.

of both circuits determines that

$$C_B(\omega) = C_1(\omega)\left[\frac{R_2^2(\omega)}{(R_2(\omega)+R_S)^2+\omega^2R_2^2(\omega)R_S^2C_1^2(\omega)}\right]$$
$$R_B(\omega) = \frac{(R_2(\omega)+R_S)^2+\omega^2R_2^2(\omega)R_S^2C_1^2(\omega)}{(R_2(\omega)+R_S)+\omega^2R_2^2(\omega)R_SC_1^2(\omega)}. \quad \text{(A1)}$$

Furthermore, it can be shown that if R_S is small enough to obey the following constraints,

$$R_S \ll \min\left[\frac{1}{\omega C_1(\omega)}, \frac{1}{\omega C_2(\omega)}, \frac{1}{\omega C_1(\omega)}\frac{C_2(\omega)}{C_1(\omega)}\right], \quad \text{(A2)}$$

then Eq. (A1) reduces to $C_B(\omega) = C_1(\omega)$ and $R_B(\omega) = R_2(\omega) = 1/[\omega C_2(\omega)]$. Alternatively, these equalities can be assumed a priori, resulting in the modified, measureable constraints

$$R_S \ll \min\left[\frac{1}{\omega C_B(\omega)}, R_B, \frac{1}{\omega^2 C_B^2(\omega)R_B}\right], \quad \text{(A3)}$$

which, if satisfied experimentally, prove the assumptions true. These constraints are satisfied over our entire measurement bandwidth, ensuring the ac dissipation is due to dielectric loss, and that the in-plane voltage drop across the series resistance R_S can be ignored (see Ref. 18).

With R_S and R_0 effectively removed from the circuit, all that remains is the complex capacitance $C^*(\omega) = C_1(\omega) - iC_2(\omega)$. However, considering this capacitance as a general complex impedance, we can further specify its components. The capacitance of our sample is actually the result of a modified Maxwell-Wagner circuit, as illustrated in Fig. 9(c), where the complex manganite capacitance (and its leakage resistor R_M), are in series to a leakage-free and dispersionless real capacitance of the AlO_x layer C_{AlOx}.

3. Circuit approximations

As discussed in the previous sections, the circuit model which represents our sample has been simplified to the modified Maxwell-Wagner circuit shown in Fig. 9(c). The analytical expression for the effective capacitance of this

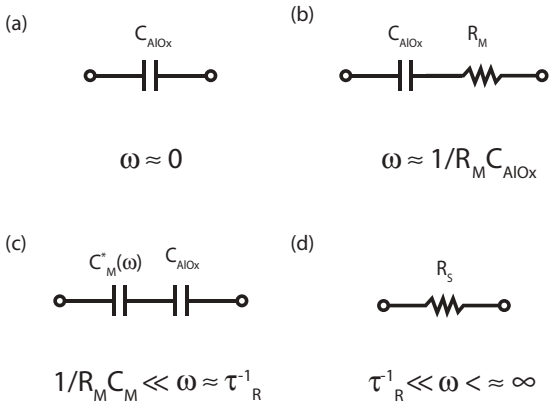

FIG. 10. Circuit approximations at select time scales. (a) At dc the entire voltage drop is across the AlO_x capacitor [see Fig. 8(b)]. (b) When $\omega \approx 1/R_M C_{AlOx}$, the circuit simplifies to a series combination of the AlO_x capacitance and manganite resistance. (c) When $\omega \ll 1/R_M C_M$, this is approximated by a series combination of the AlO_x capacitance and manganite capacitance. (d) At very high frequencies the constraints of Eq. (A3) fail and the in-plane voltage drop across the series resistance dominates, reducing the circuit to the series resistance.

circuit is given by Eq. (1), which we repeat here:

$$C^* = \frac{C_{AlO_x}}{1 + \left(i\omega R_M C_{AlO_x}\right)/(1 + i\omega R_M C_M)}. \quad \text{(A4)}$$

However, because we measure the complex capacitance as a function of frequency, this circuit can be approximated by even simpler circuits by considering specific time scales. As shown in Fig. 8(b), when $\omega \approx 0$ the equipotentials are concentrated in the AlO_x layer, and the circuit can be approximated by C_{AlOx} alone [see Fig. 10(a)]. As the frequency is increased, and $\omega \approx 1/R_M C_{AlOx}$, the circuit transitions to a series combination of R_M and C_{AlOx} as shown in Fig. 10(b) (this can be seen in Eq. (A4) by realizing $\omega R_M C_M \ll 1$ since $C_{AlOx} \gg C_M$). Increasing the frequency further, so that $\omega \gg 1/R_M C_M$, Eq. (1) simplifies to Eq. (2),

$$C^* = \frac{C_{AlO_x} C_M}{C_{AlO_x} + C_M}. \quad \text{(A5)}$$

This limit represents the manganite and AlO_x capacitors connected in series, as shown in Fig. 10(c). Because $C_{AlOx} \gg C_M$, this circuit is dominated by C_M, so that $C^* \approx C_M$. Prior to this frequency range C_M can be approximated as real and dispersionless, however, at high enough frequency the inherent relaxation of the manganite dielectric response at characteristic relaxation times τ_R becomes relevant ($\omega \approx 1/\tau_R$), and both components of C_M display frequency dependence. This is the frequency range where all of the data presented here is measured. Finally, when $\tau_R^{-1} \ll \omega$, the constraints of Eq. (A3) are no longer satisfied, meaning the voltage is confined to the in-plane series resistance, and the circuit can be represented simply by R_S as shown in Fig. 10(d).

[1] K. M. Lang, V. Madhavan, J. E. Hoffman, E. W. Hudson, H. Eisaki, S. Uchida, and J. C. Davis, Nature (London) **415**, 412 (2002).
[2] V. J. Emery, S. A. Kivelson, and H. Q. Lin, Phys. Rev. Lett. **64**, 475 (1990).
[3] J. Hemberger, P. Lunkenheimer, R. Fichtl, H.-A. Krug von Nidda, V. Tsurkan, and A. Loidl, Nature (London) **434**, 364 (2005).
[4] M. P. Singh, W. Prellier, L. Mechin, and B. Raveau, Appl. Phys. Lett. **88**, 012903 (2006).
[5] S. Danjoh, J.-S. Jung, H. Nakamura, Y. Wakabayashi, and T. Kimura, Phys. Rev. B **80**, 180408(R) (2009).
[6] M. Uehara, S. Mori, C. H. Chen, and S.-W. Cheong, Nature (London) **399**, 560 (1999).
[7] Casey Israel1, Amlan Biswas, R. L. Greene, and Alex de Lozanne, Science **298**, 805 (2002).
[8] J. Burgy, A. Moreo, and E. Dagotto, Phys. Rev. Lett. **92**, 097202 (2004).
[9] K. Ahn, T. Lookman, and A. Bishop, Nature (London) **428**, 401 (2004).
[10] G. Milward, M. Calderon, and P. Littlewood, Nature (London) **433**, 607 (2005).
[11] E. Dagotto, Science **309**, 257 (2005).
[12] A. Banerjee, A. K. Pramanik, Kranti Kumar, and P. Chaddah, J. Phys.: Condens. Matter **18**, L605 (2006).
[13] A. Nucara, P. Maselli, P. Calvani, R. Sopracase, M. Ortolani, G. Gruener, M. Cestelli Guidi, U. Schade, and J. García, Phys. Rev. Lett. **101**, 066407 (2008).
[14] Tara Dhakal, Jacob Tosado, and Amlan Biswas, Phys. Rev. B **75**, 092404 (2007).
[15] H. J. Lee, K. H. Kim, M. W. Kim, T. W. Noh, B. G. Kim, T. Y. Koo, S.-W. Cheong, Y. J. Wang, and X. Wei, Phys. Rev. B **65**, 115118 (2002).
[16] V. Kiryukhin, B. G. Kim, V. Podzorov, S.-W. Cheong, T. Y. Koo, J. P. Hill, I. Moon, and Y. H. Jeong, Phys. Rev. B **63**, 024420 (2000).
[17] J. Tao and J. M. Zuo, Phys. Rev. B **69**, 180404 (2004).
[18] Ryan P. Rairigh, Guneeta Singh-Bhalla, Sefaatin Tongay, Tara Dhakal, Amlan Biswas, and Arthur F. Hebard, Nat. Phys. **3**, 551 (2007).
[19] A. K. Jonscher, Nature (London) **267**, 673 (1977).
[20] K. S. Cole and R. H. Cole, J. Chem. Phys. **9**, 341 (1941).
[21] M. Salamon and M. Jaime, Rev. Mod. Phys. **73**, 583 (2001).
[22] R. S. Freitas, J. F. Mitchell, and P. Schiffer, Phys. Rev. B **72**, 144429 (2005).
[23] N. Bikup, A. de Andrés, J. L. Martinez, and C. Perca, Phys. Rev. B **72**, 024115 (2005).
[24] J. L. Cohn, M. Peterca, and J. J. Neumeier, Phys. Rev. B **70**, 214433 (2004).
[25] W. Prellier, Ch. Simon, A. M. Haghiri-Gosnet, B. Mercey, and B. Raveau, Phys. Rev. B **62**, R16337 (2000).
[26] Susan Cox, J. Singleton, R. D. McDonald, A. Migliori, and P. B. Littlewood, Nat. Mater. **7**, 25 (2008).
[27] A. Nucara, P. Maselli, P. Calvani, R. Sopracase, M. Ortolani, G. Gruener, M. Cestelli Guidi, U. Schade, and J. García, Phys. Rev. Lett. **101**, 066407 (2008).

[28]C. Barone, A. Galdi, N. Lampis, L. Maritato, F. Miletto Granozio, S. Pagano, P. Perna, M. Radovic, and U. Scotti di Uccio, Phys. Rev. B **80**, 115128 (2009).
[29]N. P. Ong, J. W. Brill, J. C. Eckert, J. W. Savage, S. K. Khanna, and R. B. Somoano, Phys. Rev. Lett. **42**, 811 (1979).
[30]P. Chaikin, W. W. Fuller, R. LaCoe, J. F. Kwak, R. L. Greene, J. C. Eckert, and N. P. Ong, Solid State Commun. **39**, 553 (1981).
[31]S. Bhattacharya, J. P. Stokes, M. J. Higgins, and R. A. Klemm, Phys. Rev. Lett. **59**, 1849 (1987).
[32]S. Havrilia and S. Negami, Polymer **8**, 161 (1967).